Quantifying Microstructure in Fiber Crossings with Diffusional Kurtosis

Michael Ankele and Thomas Schultz

University of Bonn, Germany⋆

Abstract. Diffusional Kurtosis Imaging (DKI) is able to capture non-Gaussian diffusion and has become a popular complement to the more traditional Diffusion Tensor Imaging (DTI). In this paper, we demonstrate how strongly the presence of fiber crossings and the exact crossing angle affect measures from diffusional kurtosis, limiting their interpretability as indicators of tissue microstructure. We alleviate this limitation by modeling fiber crossings with a mixture of cylindrically symmetric kurtosis models. Based on results on simulated and on real-world data, we conclude that explicitly including crossing geometry in kurtosis models leads to parameters that are more specific to other aspects of tissue microstructure, such as scale and homogeneity.

1 Introduction

Diffusional Kurtosis Imaging (DKI) is a natural and popular extension of Diffusion Tensor Imaging (DTI) that accounts for the empirically observed non-Gaussianity of diffusion in biological tissue. Measures of diffusional kurtosis are known to be affected by factors such as the scale and homogeneity of obstacles to the molecular motion [4], and therefore provide useful information on tissue microstructure, complementing the information captured in the diffusion tensor.

Many studies of white matter are motivated by an interest in structural parameters, such as nerve fiber density or myelination. They use diffusion MRI because it provides quantities that are affected by such factors, and that are easy and safe to obtain *in vivo*. A known limitation of diffusion tensor imaging is the fact that measures such as fractional anisotropy are sensitive, but not specific to those parameters of interest: The effect of confounding factors, such as the presence of orientational dispersion or fiber crossings, can be substantial.

In Section 3 of this paper, we discuss an analogous limitation in DKI: We show that common measures of diffusional kurtosis are not specific to microstructural parameters of individual fibers, but are heavily affected by the presence, and the exact angle, of fiber crossings. This motivates development of a novel computational method in Section 4, in which the impact of those nuisance parameters is

greatly reduced. Its building block is a cylindrically symmetric kurtosis model. In Section 5, we present results on simulated data, confirming that our newly derived kurtosis measures are affected far less by the crossing angle than results of traditional DKI. We also show parameter maps that demonstrate the effectiveness of our method on real data.

2   Related Work

Several recent works have aimed to reduce the effects of fiber crossings and orientational dispersion on quantitative markers from diffusion MRI. NODDI disentangles the effects of neurite orientation dispersion and density, but does not model fiber crossings [16]. Spherical deconvolution can be used to quantify fiber properties in a way that is robust to fiber crossings, either by analyzing the fiber orientation distribution function after using a fixed deconvolution kernel [8,2], or by calibrating the kernel itself [10]. Finally, estimation of per-compartment diffusion parameters can be integrated into crossing-fiber tractography [6,9].

Our work is most closely related to a series of approaches that have fitted multiple diffusion tensors [15,5,13]. However, none of them model diffusional kurtosis. We demonstrate how fiber crossings affect kurtosis measures and propose novel kurtosis measures whose sensitivity to crossings is greatly reduced.

3   How Fiber Crossings Affect Diffusional Kurtosis

It is well-known that fiber crossings strongly affect measures derived from the diffusion tensor model, such as Fractional Anisotropy (FA). It is unsurprising that the same is true for measures of diffusional kurtosis. Our first goal is to systematically demonstrate the exact extent of this dependence.

We have synthesized crossings with varying crossing angles between 0 and 90 degrees, and created plots of how diffusional kurtosis depends on it. Signal synthesis was performed in a data-driven manner from a subject from the Human Connectome Project (288 DWIs on shells at $b \approx \{5, 1000, 2000, 3000\}$ s/mm^2). It is based on 300 voxels thought to contain a single dominant fiber compartment, given as the voxels with highest FA within a white matter mask. The DKI model was fit to the data, and model parameters were analytically rotated by the desired crossing angle. Diffusion-weighted signals were computed from the original and rotated model, and averaged. This simulates two fiber compartments that cross at a known angle, with no significant exchange within the diffusion time. Since we use the full DKI model, it does not impose cylindrical symmetry.

We performed a constrained least squares fit of the diffusional kurtosis model to the simulated data [12]. Fig. 1 plots mean and one standard deviation of the resulting mean, axial, and radial kurtosis, over the 300 voxels used to simulate the crossings. The plots in the top row show that the dependence on the crossing angle is substantial: Compared to the baseline (value for a single fiber compartment, indicated by a green line), the crossing changes radial kurtosis by a factor of up to 4.23, and axial kurtosis up to 5.65. A very similar dependence
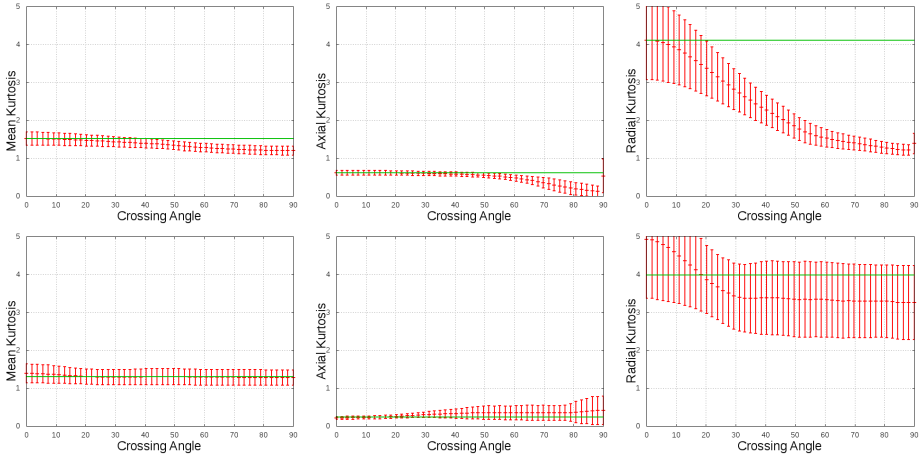
Fig. 1. *Top:* The angle at which fibers cross has a severe impact on the parameters of DKI. *Bottom:* The proposed model reduces effects of crossing geometry, leading to biomarkers that more specifically quantify microstructure properties.

is observed for axial and radial diffusivities (not shown). Studies that aim to use kurtosis to specifically quantify microstructure properties, without confounding effects from crossings, should be aware of this problem. We will now introduce a method to compute novel kurtosis measures, shown in the lower row of Fig. 1, that are less susceptible to the undesired impact of crossing geometry.

4   A Mixture of Kurtosis Models

The general strategy of our method is to fit a mixture of kurtosis models to fiber crossings. In effect, this adds kurtosis to previous methods that have modeled fiber crossings using multiple diffusion tensors.

4.1   A Cylindrically Symmetric Kurtosis Model

The full kurtosis model has six parameters for the diffusion tensor, plus 15 for the kurtosis tensor. This seems prohibitive for fitting a mixture. We thus constrain the kurtosis models that will represent the individual fiber compartments in our mixture to be cylindrically symmetric around the principal diffusion direction.

The same symmetry is frequently assumed in multi-tensor models [15,5]. It reduces the 21 parameters in the full kurtosis model to only 7: Two angles that parameterize a unit vector $\mathbf{v}$ indicating the fiber direction, axial and radial diffusivities $(\lambda_{\parallel}, \lambda_{\perp})$, as well as three kurtosis-related parameters: In addition to $\kappa_{\parallel}$ and $\kappa_{\perp}$, which are related to axial and radial kurtosis, the fact that kurtosis is a fourth-order quantity introduced a third parameter $\kappa_{\diamond}$. The resulting signal equation as a function of gradient direction $\mathbf{g}$ and b value is

$$\ln \frac{S_{cyl}(\mathbf{g}, b; \mathbf{v})}{S_0} = -b \left[\lambda_\perp + (\lambda_\parallel - \lambda_\perp) \langle \mathbf{v}, \mathbf{g} \rangle^2 \right] +$$
$$\frac{b^2}{6} \left[\kappa_\perp + (\kappa_\diamond - 2\kappa_\perp) \langle \mathbf{v}, \mathbf{g} \rangle^2 + (\kappa_\parallel - \kappa_\diamond + \kappa_\perp) \langle \mathbf{v}, \mathbf{g} \rangle^4 \right]$$
(1)

To simplify Eq. (1), κ_* absorb the square of the mean diffusivity $\bar{\lambda} = (\lambda_\parallel + 2\lambda_\perp)/3$ that usually occurs as a factor in diffusional kurtosis. This means that axial and radial kurtosis K_* can be computed from our parameters as

$$K_\parallel = \frac{\kappa_\parallel}{\lambda_\parallel^2} \qquad \text{and} \qquad K_\perp = \frac{\kappa_\perp}{\lambda_\perp^2}.$$
(2)

Assuming that the fiber is oriented along the z axis, our model parameters translate to a standard kurtosis tensor via

$$W_{xxxx} = W_{yyyy} = 3W_{xxyy} = \frac{\kappa_\perp}{\bar{\lambda}^2}, \ W_{xxzz} = W_{yyzz} = \frac{\kappa_\diamond}{6\,\bar{\lambda}^2}, \ W_{zzzz} = \frac{\kappa_\parallel}{\bar{\lambda}^2}.$$
(3)

This allows computation of mean kurtosis MK using the equations given in [12].

We have used the Bayesian Information Criterion (BIC) to compare our cylindrically symmetric model with two variants, one with a ball compartment, the other one with a dot compartment [7], and with the full kurtosis model. Ranking them with respect to their BIC preferred "symmetric+dot" in 96.3% of all cases, "symmetric" in 3.0%, the full kurtosis model in 0.7%, and "symmetric+ball" in 0%. Therefore, we include a dot compartment in all our experiments.

4.2 Strategy for Fitting the Final Mixture

Our final signal equation results from using Eq. (1) to model each of k crossing fiber compartments and adding the dot compartment:

$$S(\mathbf{g}, b) = S_0 \left[f_{dot} + \sum_{i=1}^{k} f_i S_{cyl}(\mathbf{g}, b; \mathbf{v}_i) \right]$$
(4)

Volume fractions f_* are constrained to be non-negative, and to add to one. We ensure numerical stability in evaluating Eq. (2), and force $\mathbf{v}_i$ to align with a principal diffusion direction, by constraining $\lambda_\perp \in [0.01\lambda_\parallel, \lambda_\parallel]$ and $\lambda_\parallel > \epsilon$. We also impose the same constraints on our kurtosis parameters as Tabesh et al., $3/(b_{max}\lambda) \geq K \geq 0$ [12]. As in the widely used ball-and-stick model [1], the diffusion and kurtosis parameters of all compartments are coupled. Trying to obtain stable estimates without this constraint is a topic for future work.

Even though Eq. (4) is relatively straightforward conceptually, fitting it to a given set of measurements amounts to a difficult non-convex optimization problem. We have developed the following strategy for solving it: A suitable initialization is obtained from a diffusion tensor fit, by setting $\lambda_\parallel$ to the largest eigenvalue and $\lambda_\perp$ to the mean of the two smaller ones. Fiber volume fractions f_i and directions $\mathbf{v}_i$ are initialized by discretizing an orientation distribution function from spherical deconvolution, as proposed in [11]. The kurtosis parameters and f_{dot} are initialized to zero.

Table 1. Statistics on the difference between kurtosis estimates in simulated crossings and the single fiber voxels from which they were generated quantify the extent to which we reduce the impact of crossings. At low SNR, neither model gives useful results.

SNR	Kurtosis Tensor Model			Our Kurtosis Mixture Model		
	MK	$K_{\parallel}$	$K_{\perp}$	MK	$K_{\parallel}$	$K_{\perp}$
∞	-0.15 ± 0.17	-0.09 ± 0.22	-1.69 ± 1.60	-0.00 ± 0.07	0.02 ± 0.07	-0.20 ± 1.01
40	-0.15 ± 0.28	-0.09 ± 0.21	-1.75 ± 1.76	0.01 ± 0.31	0.02 ± 0.08	-0.14 ± 1.62
30	-0.15 ± 0.28	0.17 ± 0.38	-1.95 ± 1.36	0.16 ± 0.40	0.20 ± 0.50	-0.36 ± 1.48
20	-0.04 ± 0.45	0.35 ± 0.51	-1.89 ± 1.35	0.42 ± 0.84	0.52 ± 1.00	-0.27 ± 1.95
10	0.49 ± 1.18	0.83 ± 0.96	-1.43 ± 2.02	1.79 ± 5.05	1.61 ± 2.52	1.88 ± 14.90

The fitting itself is performed with constrained Levenberg-Marquardt optimization. We found that it can be accelerated greatly by re-parametrizing diffusivity and kurtosis parameters. The actual parameters visible to the optimizer are $\ln(\lambda_{\parallel})$, $\lambda_{\perp}/\lambda_{\parallel}$, $1000\kappa_{\parallel}/\lambda_{\parallel}$, $1000\kappa_{\perp}/\lambda_{\perp}$, $1000\kappa_{\diamond}/\lambda_{\parallel}$. Moreover, we observed that convergence benefits from splitting the parameters into two blocks, and alternating between their optimization. The first block contains the volume fractions and directions, which we parameterize using elevation and azimuth angles. The second block optimizes diffusion and kurtosis. Despite these optimization, processing a slice of 174×145 voxels on 6 cores of a 3.4GHz $i7$ takes 6 minutes.

5   Results

5.1   Simulated Data

As an initial validation of our model and fitting procedure, we applied it to the simulated data that was described in Section 3. The results are shown in the bottom row of Fig. 1. They confirm that our crossing model succeeds in absorbing a significant part of the variation in kurtosis measures which is otherwise caused by crossing geometry. The results remain much closer to the baseline, which is indicated by the green line. Note that differences between the baselines in both rows are due to the presence of the dot compartment.

For a quantitative summary, we have taken the difference of kurtosis parameters estimated in the crossing by the two models, and a baseline, computed by the same method from the single-fiber voxel that was used to simulate the fiber crossing. Table 1 reports the mean and standard deviation of this difference over all 300 voxels and all crossing angles. It confirms that our model greatly reduces the impact of crossings, in particular in case of radial kurtosis. The relatively low standard deviations indicate that fitting works reliably. Table 1 also shows the results of adding Rician noise to the simulation, indicating that our fitting starts to degrade around SNR $\approx$ 20. At this point, even values from the full model start to exhibit a noticeable bias.

5.2   Real Data

In addition to the quantitative validation on simulated data, we have verified that our model produces plausible results on real human brain scans by fitting
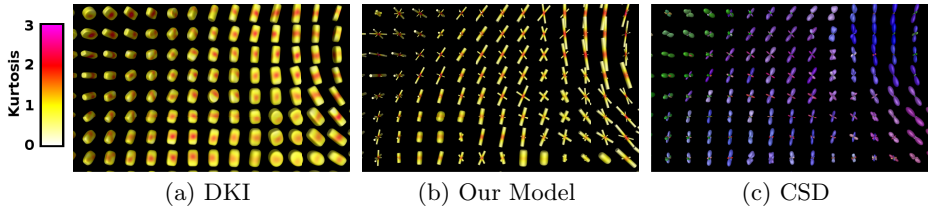
Fig. 2. Our mixture of cylindrically symmetric kurtosis compartments (b) results in principal fiber directions that agree well with constrained spherical deconvolution (c). In contrast to the traditional kurtosis model (a), it leads to measures that disentangle the effects of microstructure and crossing geometry.

it to data from the human connectome project. In each voxel, the BIC has been used to select between models with a single, two, or three cylindrically symmetric kurtosis compartments.

A detail of the result on a coronal slice, in the region where fibers from the corpus callosum, corticospinal tract, and superior longitudinal fasciculus cross, is visualized in Fig. 2 using superquadric glyphs [3] for the diffusion tensor part of the kurtosis model. Glyphs have been scaled with the volume fraction of the respective compartment, and color coded with directional kurtosis. In contrast to the traditional kurtosis model in (a), directions of crossing fibers are immediately apparent from our result (b).

A comparison to the widely used constrained spherical deconvolution model [14], which we fitted to the subset of measurements with $b \approx 3000 \, \text{s/mm}^2$, is shown in Fig. 2 (c). The agreement of principal fiber directions and relative volume fractions confirms that the individual kurtosis compartments in our model successfully capture the dominant fiber populations in real crossings.

However, our main interest is in the kurtosis measures themselves, which are mapped in the bottom row of Fig. 3 and compared to the corresponding ones from standard kurtosis imaging in the top row. MK and $K_\parallel$ are mapped with range $[0, 2]$; $K_\perp$ is mapped with range $[0, 5]$; FA is shown with range $[0, 1]$.

Within the white matter, our model measures a much lower $K_\parallel$ than the classical DKI model, close to that of free diffusion. In gray matter, our $K_\parallel$ remains high, providing a clear contrast between the two tissue types. This correlates with the volume fraction of the dot compartment; after factoring it out, MK is nearly uniform over the brain tissue (Fig. 3 (e)).

$K_\perp$ and FA have been computed from the diffusion tensors of both models. There is a clear visual similarity between structures in Fig. 3 (c) and (d), which is much reduced in the corresponding Fig. 3 (g) and (h): While the FA from our model remains high throughout the white matter (in agreement with the results in [10]), confirming the reduced impact of fiber crossings, our radial kurtosis still shows substantial variation, which reflects more subtle aspects of tissue architecture. We believe that the similarity between Fig. 3 (c) and (d) is caused by the fact that, in standard DKI, FA and $K_\perp$ are both reduced in regions of fiber crossings, and that factoring out the effect of crossings emphasizes the information specific to diffusional kurtosis.
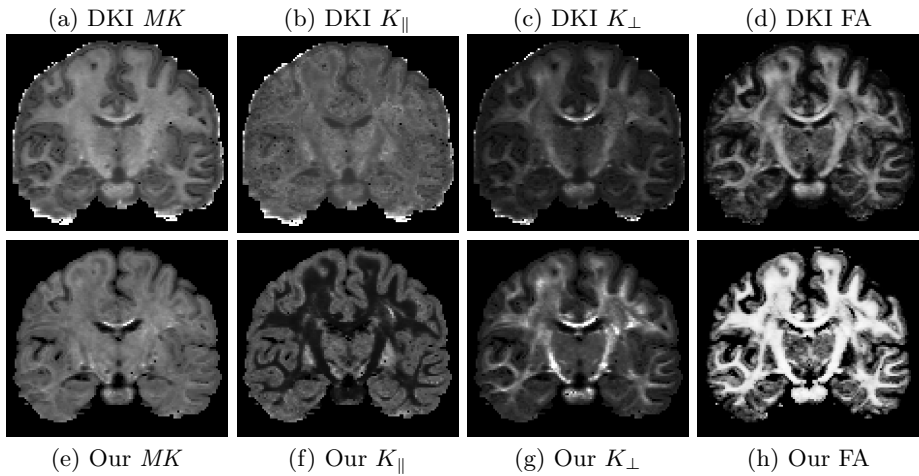
(a) DKI *MK*   (b) DKI $K_{\parallel}$ (c) DKI $K_{\perp}$ (d) DKI FA

(e) Our *MK*   (f) Our $K_{\parallel}$ (g) Our $K_{\perp}$ (h) Our FA

Fig. 3. Differences in *MK* and $K_{\parallel}$ between our model and standard DKI appear to be due to including a dot compartment, while those in $K_{\perp}$ and FA are more strongly affected by the reduced impact of fiber crossings.

6   Conclusion

In this work, we have demonstrated how strongly measures from diffusional kurtosis are affected by fiber crossings, which limits their interpretability as indicators of tissue microstructure. To alleviate this, we have explicitly accounted for crossings by adding a cylindrically symmetric kurtosis term to the popular multi-tensor model. Results on simulated data confirm that the resulting model remains tractable, and successfully disentangles the effects of crossings and per-compartment tissue parameters.

In real data, the maps from our model differ significantly from standard diffusional kurtosis imaging; we believe that they more specifically indicate factors such as scale and homogeneity of tissue microstructure. As a next step, we plan to use additional simulations and a systematic comparison to other MR-derived quantities to gain more insight into the exact interpretation of these maps. We also plan to use spatial regularization to achieve stable fitting on noisy data.

References

1. Behrens, T.E.J., Johansen-Berg, H., Jbabdi, S., Rushworth, M.F.S., Woolrich, M.W.: Probabilistic diffusion tractography with multiple fibre orientations: What can we gain? NeuroImage 34, 144–155 (2007)
2. Dell'Acqua, F., Simmons, A., Williams, S.C.R., Catani, M.: Can spherical deconvolution provide more information than fiber orientations? hindrance modulated orientational anisotropy, a true-tract specific index to characterize white matter diffusion. Human Brain Mapping 34(10), 2464–2483 (2013)

3. Ennis, D.B., Kindlmann, G., Rodriguez, I., Helm, P.A., McVeigh, E.R.: Visualization of tensor fields using superquadric glyphs. Magnetic Resonance in Medicine 53(1), 169–176 (2005)
4. Jensen, J.H., Helpern, J.A.: MRI quantification of non-gaussian water diffusion by kurtosis analysis. NMR in Biomedicine 23(7), 698–710 (2010)
5. Kreher, B., Schneider, J., Mader, I., Martin, E., Hennig, J., Il'yasov, K.: Multitensor approach for analysis and tracking of complex fiber configurations. Magnetic Resonance in Medicine 54, 1216–1225 (2005)
6. Malcolm, J.G., Shenton, M.E., Rathi, Y.: Filtered multitensor tractography. IEEE Trans. on Medical Imaging 29(9), 1664–1675 (2010)
7. Panagiotaki, E., Schneider, T., Siow, B., Hall, M.G., Lythgoe, M.F., Alexander, D.C.: Compartment models of the diffusion MR signal in brain white matter: A taxonomy and comparison. NeuroImage 59, 2241–2254 (2012)
8. Raffelt, D., Tournier, J.D., Rose, S., Ridgway, G.R., Henderson, R., Crozier, S., Salvado, O., Connelly, A.: Apparent fibre density: A novel measure for the analysis of diffusion-weighted magnetic resonance images. NeuroImage 59(4), 3976–3994 (2012)
9. Reisert, M., Kiselev, V.G., Dihtal, B., Kellner, E., Novikov, D.S.: MesoFT: unifying diffusion modelling and fiber tracking. In: Golland, P., Hata, N., Barillot, C., Hornegger, J., Howe, R. (eds.) MICCAI 2014, Part III. LNCS, vol. 8675, pp. 201–208. Springer, Heidelberg (2014)
10. Schultz, T., Groeschel, S.: Auto-calibrating spherical deconvolution based on ODF sparsity. In: Mori, K., Sakuma, I., Sato, Y., Barillot, C., Navab, N. (eds.) MICCAI 2013, Part I. LNCS, vol. 8149, pp. 663–670. Springer, Heidelberg (2013)
11. Schultz, T., Westin, C.F., Kindlmann, G.: Multi-diffusion-tensor fitting via spherical deconvolution: A unifying framework. In: Jiang, T., Navab, N., Pluim, J.P.W., Viergever, M.A. (eds.) MICCAI 2010, Part I. LNCS, vol. 6361, pp. 673–680. Springer, Heidelberg (2010)
12. Tabesh, A., Jensen, J.H., Ardekani, B.A., Helpern, J.A.: Estimation of tensors and tensor-derived measures in diffusional kurtosis imaging. Magnetic Resonance in Medicine 65, 823–836 (2011)
13. Taquet, M., Scherrer, B., Boumal, N., Macq, B., Warfield, S.K.: Estimation of a multi-fascicle model from single b-value data with a population-informed prior. In: Mori, K., Sakuma, I., Sato, Y., Barillot, C., Navab, N. (eds.) MICCAI 2013, Part I. LNCS, vol. 8149, pp. 695–702. Springer, Heidelberg (2013)
14. Tournier, J.D., Calamante, F., Connelly, A.: Robust determination of the fibre orientation distribution in diffusion MRI: Non-negativity constrained super-resolved spherical deconvolution. NeuroImage 35, 1459–1472 (2007)
15. Tuch, D.S., Reese, T.G., Wiegell, M.R., Makris, N., Belliveau, J.W., Wedeen, V.J.: High angular resolution diffusion imaging reveals intravoxel white matter fiber heterogeneity. Magnetic Resonance in Medicine 48, 577–582 (2002)
16. Zhang, H., Schneider, T., Wheeler-Kingshott, C.A., Alexander, D.C.: NODDI: practical in vivo neurite orientation dispersion and density imaging of the human brain. NeuroImage 61(4), 1000–1016 (2012)